Supporting Information

Stable Alkali Metal Ion Intercalation Compounds as Optimized Metal Oxide Nanowire Cathodes for Lithium Batteries

Yunlong Zhao,[†,∥,#] Chunhua Han,[†,#] Junwei Yang,[‡,#] Jie Su,[§] Xiaoming Xu,[†] Shuo Li,[†] Lin Xu,[∥]

Ruopian Fang,[†] Hong Jiang,[⊥] Xiaodong Zou,[*,§] Bo Song,[*,‡] Liqiang Mai,[*,†] and Qingjie Zhang[†]

Part 1. Supplementary Information of Methods

1. Synthesis of A-M-O (M = V, Mo, Co, Mn, Fe-P).

A-V-O:

The A-V-O (A= Li, Na, K, Rb) samples were prepared through a hydrothermal process combined with an annealing treatment afterwards. In a typical synthesis, 0.100 g of polyethyleneglycol (PEG-4000), 0.1818 g of V_2O_5 powder (high purity, Wako) and 0.35 ml of AOH (1 mol/L, A= Li, Na, K) for A-V-O (A= Li, Na, K) or 0.70 ml AOH (1 mol/L, A= Rb) for A-V-O (A = Rb) were added in 30 mL of deionized water under vigorous magnetic stirring at room temperature for 2 h. The resultant mixture was then transferred to a 50 mL autoclave and maintained in an oven at 180 ^{o}C for 48 h. After the sample was cooled to room temperature naturally, the product was washed with deionized water and anhydrous alcohol several times and dried at 70 ^{o}C in an air oven. After that, the dried sample of Li-V-O was annealed at 300 ^{o}C in air for 0.25 h first, after cooling to room temperature, a second annealing process at 350 ^{o}C in air for 3 h was performed; for A-V-O (A=Na, K, Rb), the dried sample was annealed in air (Na-V-O at 500 ^{o}C for 5 h; K-V-O at 550 ^{o}C for 3 h; Rb-V-O at 500 ^{o}C for 10 h) to obtained the final products.

A-Mo-O:

For A-Mo-O (A=Li, Na, K, Rb), the synthetic process is as follow: α-MoO_3 nanowires were synthesized by a hydrothermal method firstly, then α-MoO_3 nanowires were mixed with PEG and alkali chloride (ACl, A=Li, Na, K, Rb) stoichiometrically and homogeneously in deionized water. The resultant mixture was then transferred to a 100 mL Teflon-lined autoclave for the second hydrothermal treatment. After the sample was cooled to room temperature naturally, the product was washed with

deionized water and anhydrous alcohol several times and dried at room temperature under vacuum condition. The dried sample was finally annealed at 400 °C in air to obtain the A-Mo-O.

A-Co-O:

For A-Co-O (A=Li, Na, K, Rb), the synthetic process is as follow: Co_3O_4 nanoparticles were synthesized by a solvothermal method firstly. Cobalt acetate and PVP in ethylene glycol solvent were dried at 80 °C, annealed 2 hours at 400 °C in air, then the nanoparticles were mixed with A_2CO_3 (A=Li, Na, K, Rb) stoichiometrically and homogeneously in ethanol. The dried sample was finally annealed at 800 °C in air to obtain the A-Co-O.

A-Mn-O:

For A-Mn-O (A=Li, Na, K, Rb), the synthetic process is as follow: The precursor $MnCO_3$ were synthesized by a hydrothermal method firstly, then $MnCO_3$ were mixed and ball-milled with alkali hydroxide (AOH, A=Li, Na, K, Rb) stoichiometrically. The dried sample was annealed at 800 °C in air to obtain the A-Mn-O.

A-Fe-P-O:

For A-Fe-P-O (A=Li, Na, K, Rb), the synthetic process is as follow: ANO_3 (A=Li, Na, K, Rb) and $FeCl_2 \cdot H_2O$ were dissolved in deionized H_2O with citric acid (CA) stoichiometrically and homogeneously. Then ethylene glycol (EG) and the solution containing $NH_4H_2PO_4$ were added into the above solution. The temperature was raised again to 60 °C for 24 h to evaporate H_2O. Then the $A-FePO_4$ precursor was heated at 600 °C for 1 h in N_2 to obtain the A-Fe-P-O.

2. **Characterization.**

Powder X-ray diffraction (PXRD) patterns of Na-V-O, K-V-O and Rb-V-O samples were collected on a PANalytical X'Pert PRO MPD diffractometer in transmission geometry using Cu Kα radiation. The sample was packed into 0.5 mm borosilica capillary. The PXPD pattern of Li-V-O sample was performed on a PANanalytical X'Pert PRO diffractometer in Bragg-Brentano geometry equipped with a Pixel detector using Cu Kα1 (λ = 1.5406 Å) radiation. The sample was ground and dispersed on zero-background Si plates. The Rietveld refinement of the Na-V-O and K-V-O samples, and the Pawley refinement of Li-V-O and Rb-V-O were performed by using Topas Academic V4.1.

Field-emission scanning electron microscopy (FESEM) images were collected on a Hitachi S-4800 scanning electron microscope at an acceleration voltage of 10 kV.

Samples for TEM observations were crushed, dispersed in absolute ethanol and treated by ultra-sonication for 2 min. A droplet of the suspension was transferred onto a carbon-coated copper grid. Three-dimensional (3D) rotation electron diffraction (RED) data of A-V-O samples was collected at 200 kV using the software RED – data collection on a JEOL JEM2100 TEM. A single-tilt tomography sample holder was used for the data collection, which could tilt from -70 ° to +70 ° in the TEM. The electron beam was fully spread and covered the whole phosphorus screen. The aperture used for RED data collection was about 1.6 µm in diameter. Electron diffraction (ED) data were acquired in selected area electron diffraction mode, and after each goniometer tilt the position of the crystal was tracked by image mode. The step of the beam tilt was 0.40 ° and the step of the goniometer tilt was 2.0 °. The exposure time per ED frame was 0.5 s. The data processing was conducted by using the software RED – data processing, including peak search, unit cell determination, indexation of reflections and intensity extraction.

High-resolution transmission electron microscopy (HRTEM) of A-V-O samples was performed on a JEOL JEM-2100F microscope equipped with a field emission gun operated at an accelerating voltage of 200 kV. The images were recorded on a Gatan Ultrascan 1000 2k $\times$ 2k CCD camera.

Atomic absorption spectroscopy was measured by GBC Scientific Equipment Pty Ltd. Australi.

3. *Electrochemical properties.*

The electrochemical properties were tested with 2025 coin cells assembled in a glove box filled with pure argon gas. Lithium pellets were used as the anode, 1 M solution of $LiPF_6$ in ethylene carbon (EC)/dimethyl carbonate (DMC) was used as the electrolyte, and the electrodes were produced with 60% A-V-O nanowire active material, 30% acetylene black and 10% poly (tetrafluoroethylene) (PTFE). Galvanostatic charge/discharge measurements were performed with a multichannel battery testing system (LAND CT2001A). In the capacity fading calculation, highest capacity point is selected as starting point. Cyclic voltammetry (CV) was tested with an electrochemical workstation (Autolab PGSTAT 30).

4. *DFT computational details.*

The calculations were based on the density functional theory (DFT) as implemented in the Vienna *ab initio* simulation package (VASP)[1,2], within the generalized gradient approximation[3]. The exchange-correlation functional of the Perdew-Burke-Ernzerhof type for solids (PBEsol) was applied[4]. A plane-wave basis was employed with an energy cutoff of 500 eV. Core electrons were treated within the projector-augmented wave method[5,6]. The Monkhorst–Pack meshs of $3 \times 3 \times 1$ and $3 \times 3 \times 3$ k-point sampling in the Brillouin zone were applied for the layered and non-layered structures, respectively. All

geometries were optimized using the conjugate gradient (CG) method[7]. Convergence criteria were set to 1×10^{-4} eV and 0.05 eV $\cdot$Å^{-1} for energy and force, respectively.

The diffusion barrier of the A ion (A = Li, Na, K, Rb) in A-M-O was calculated by the climbing image nudged elastic band (CI-NEB) method[8,9] and the generalized solid-state nudged elastic band method (G-SSNEB) method[10], which were implemented in the Transition-State-Theory (TST) code for VASP[11]. The crystal structure deformation induced by the diffusion of the A ion was considered by using G-SSNEB method with quick-min (QM)[12] until the maximum residual force less than 0.05 eV $\cdot$Å^{-1}. Then the deformational crystal structure was fixed for further searching the barrier via the CI-NEB method together with the CG algorithm.

Part 2. Supplementary Information for electrochemical performance of A-V-O

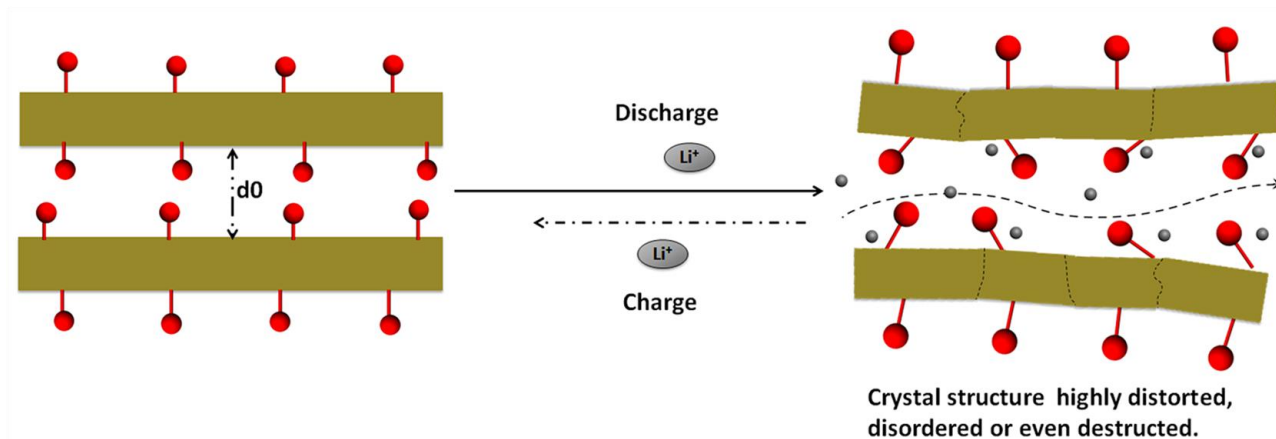*1. Crystal structure distortion, disorder and destruction during charge-discharge process:*

Figure S1. Schematic representation of some layered metal oxide cathode materials without large alkali metal ion intercalation. The crystal structure can be highly distorted, disordered or even destructed and then transform to inactive materials, which leads to poor cycling stability.
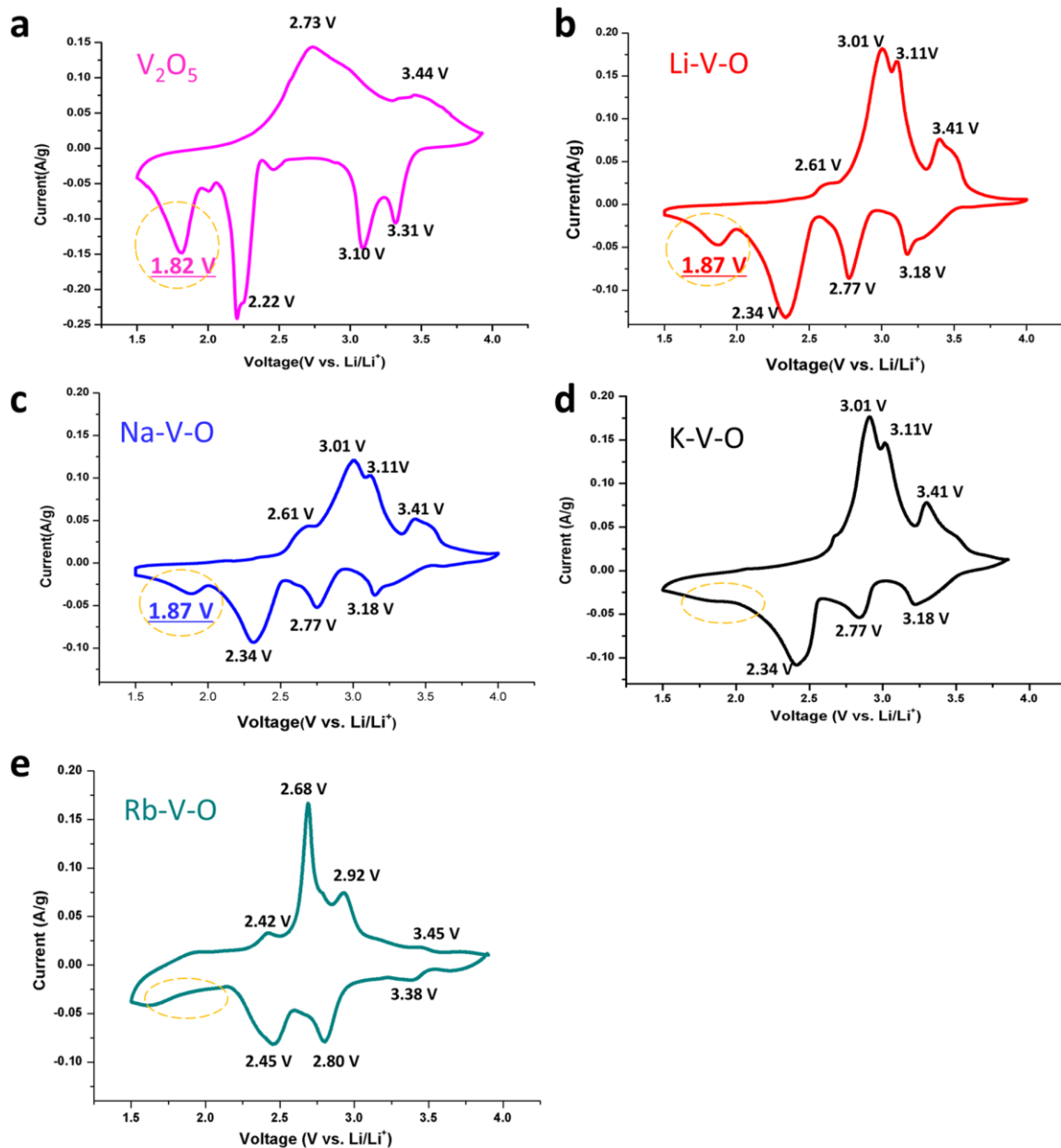
2. Cyclic voltammetry profiles of V₂O₅ and A-V-O

Figure S2. Cyclic voltammetry curves of V₂O₅ and A-V-O nanowires measured at 0.1 mV/s. (a) V₂O₅ nanowires, (b) Li-V-O nanowires, (c) Na-V-O nanowires, (d) K-V-O nanowires, (e) Rb-V-O sample. The cathodic peak at ~1.85 V, which corresponds to the only irreversible phase transition, is reduced in amplitude in the pre-intercalated materials. (Amplitude of irreversible cathodic peak: V₂O₅ >> Li-V-O > Na-V-O > Rb-V-O ≈ K-V-O).
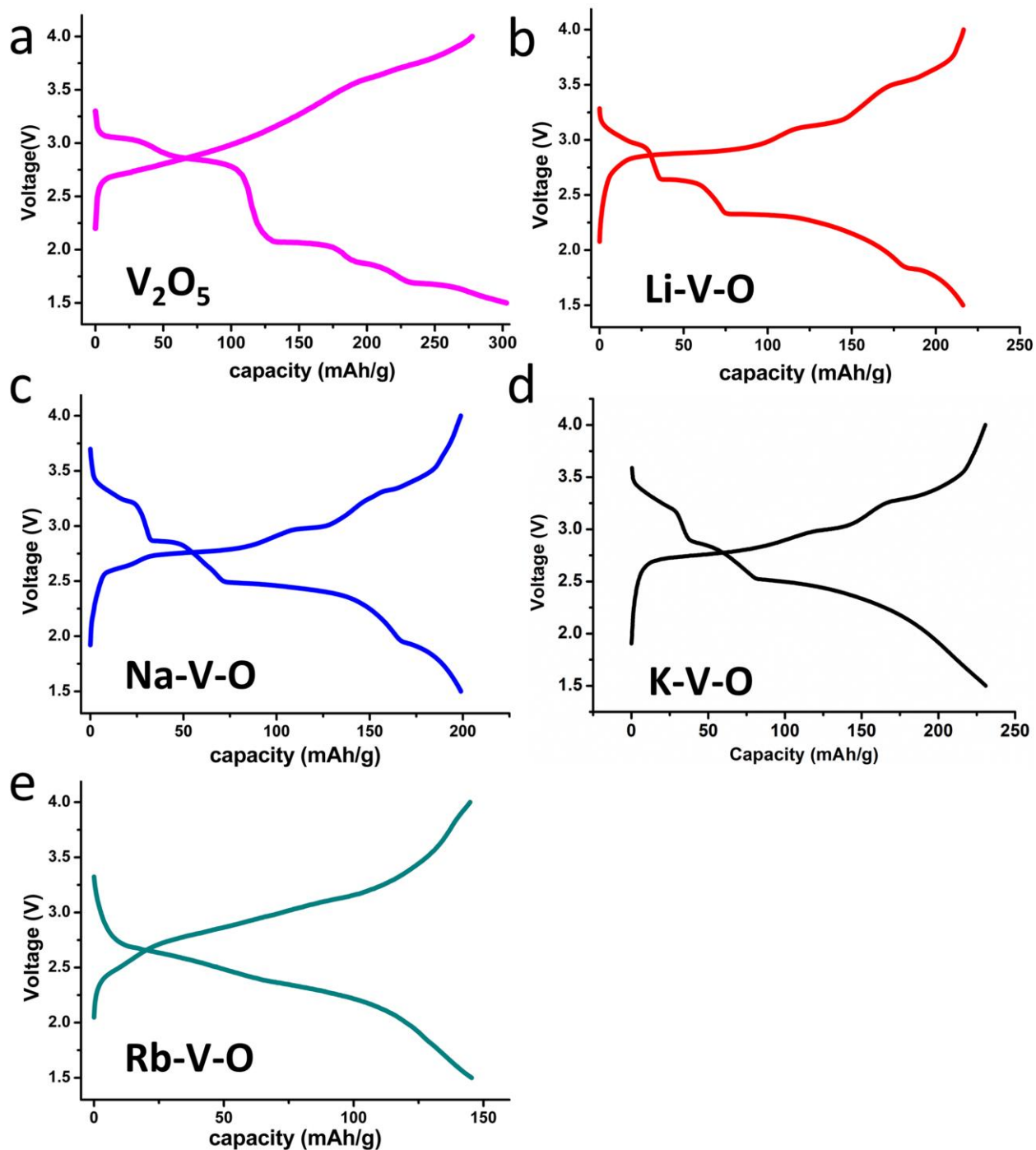
3. Charge-discharge curves of V_2O_5 and A-V-O

Figure S3. Charge-discharge curves of V_2O_5 and A-V-O nanowires measured at 100 mA/g. (**a**) V_2O_5 nanowires, (**b**) Li-V-O nanowires, (**c**) Na-V-O nanowires, (**d**) K-V-O nanowires, (**e**) Rb-V-O sample. The charge-discharge curves are consistent well with the CV curves.

Part 3. Crystallographic information and DFT computation of A-V-O
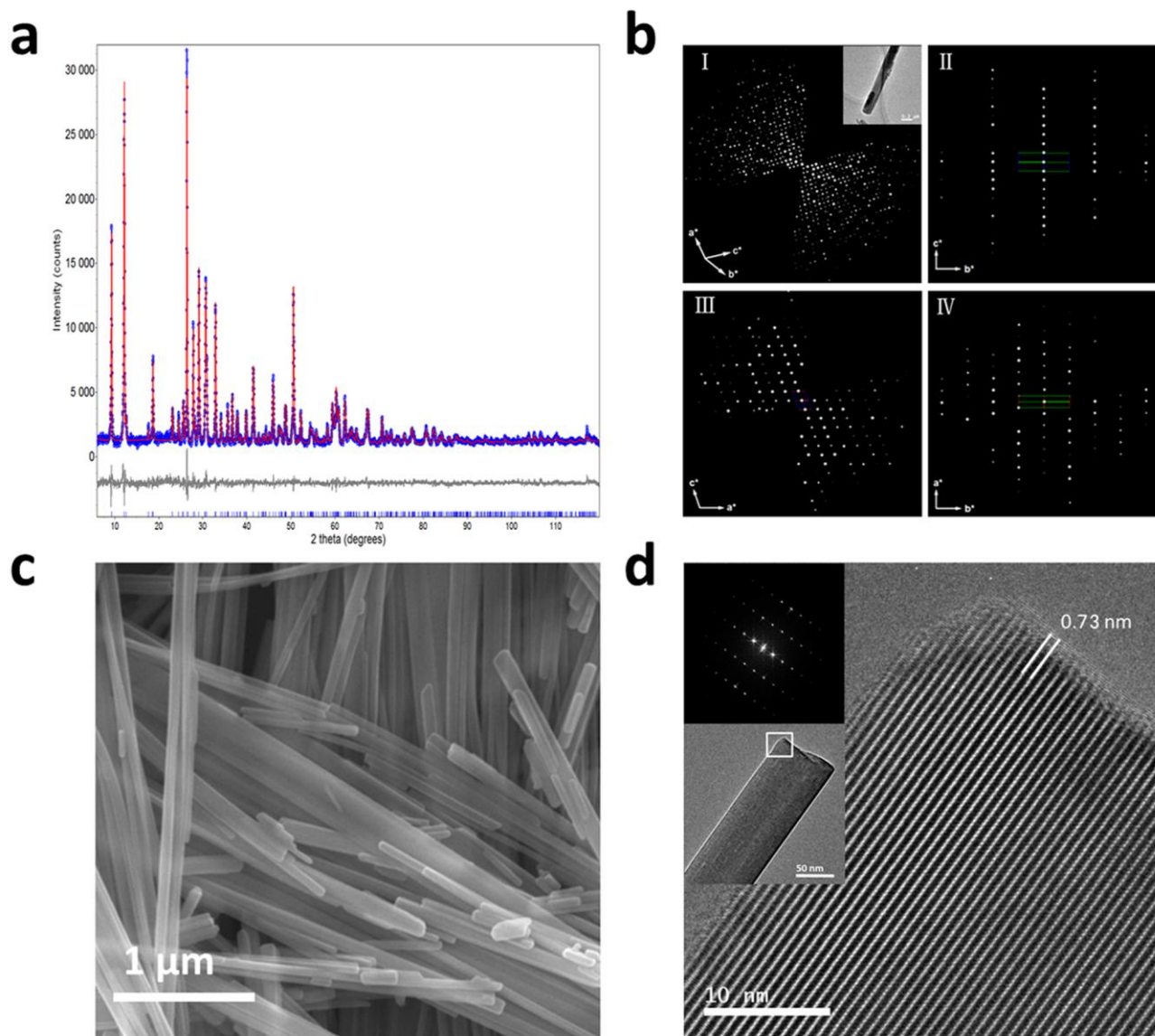
1. Na-V-O

Figure S4. Crystal structure and morphology characterization of Na-V-O nanowires. (a) Powder X-ray Rietveld refinement plot of Na-V-O nanowires. The blue circles are for the observed data. The red solid line is for the calculated data. The grey solid curve is for the difference. The vertical bars indicate positions of the Bragg peaks. (b) The rotation electron diffraction (RED) data of a Na-V-O nanowire. I represents the 3D reciprocal lattice of a Na-V-O nanowire

reconstructed from the RED data and II-IV represent 2D 0*kl*, *h*0*l* and *hk*0 slices cut from the reconstructed 3D reciprocal lattice. (**c**) SEM image of the Na-V-O nanowires. (**d**) HRTEM image from the area marked by a square in the inserted TEM image of a Na-V-O nanowire showing that the layers are in parallel to the nanowire with the layer spacing of ~ 7.3 Å. The Fourier transform of the HRTEM image is also inserted.

Table S1. Crystallographic data, experimental conditions for powder X-ray diffraction data collection and results of the Rietveld analysis of Na-V-O nanowires.

Chemical formula of framework	$Na_{0.86}V_6O_{15}$
Formula weight	565.41
Crystal system	Monoclinic
Space group	$C2/m$
a/Å	15.4082(6)
b/Å	3.6115(1)
c/Å	10.0767(3)
β/°	109.484(2)
Cell volume/Å^3	528.62(3)
Z	2
Temperature/K	298(2)
Wavelength/Å	1.5418
2ϑ range/°	6.004 - 119.989
Number of points	6706
Number of reflections	476
Number of structural variables	81
Rp	0.0698
Rwp	0.0924
Rexp	0.0240
GOF	3.841

Table S2. Atomic coordinates, thermal parameters and occupancies of Na-V-O.

Atom	x	y	z	$Beq(Å^2)$	Occupancy
V1	0.33895(21)	0	0.10237(34)	3.61(15)	1
V2	0.11781(24)	0	0.11760(27)	3.00 (13)	1
V3	0.28495(18)	0	0.40659(41)	4.00(14)	1
Na	0.0050(13)	0	0.3922(21)	4.65(72)	0.431(18)
O1	0	0	0	3.99(15)	1
O2	0.19154(84)	0	-0.0518(14)	3.99(15)	1
O3	0.36941(95)	0	-0.0734(12)	3.99(15)	1
O4	0.43977(35)	0	0.23707(55)	3.99(15)	1
O5	0.26208 (89)	0	0.2185(15)	3.99(15)	1
O6	0.10370(39)	0	0.27644(45)	3.99(15)	1
O7	0.2490(10)	0	0.5722(11)	3.99(15)	1
O8	0.39986(32)	0	0.48167 (99)	3.99(15)	1

The PXPD pattern of Na-V-O nanowires for Rietveld refinement was collected on a PANalytical X'Pert PRO MPD diffractometer in transmission geometry using Cu K_α radiation with the range 2θ = 6-120 °. The sample was packed into 0.5 mm diameter borosilica capillary. The Rietveld refinement was performed by using Topas Academic V4.1. The structure of $Na_{0.85}V_6O_{15}$ was used as the starting model for the refinement.

The rotation electron diffraction (RED) method was also applied on the Na-V-O sample. 280 ED frames were collected with a step size of 0.40 °, covering a tilt range from -50.61 ° to 62.43 °. The

exposure time for each ED frame was 0.5 s. The three-dimensional reciprocal lattice was reconstructed from the ED frames using the RED software package and is shown in Figure S4B. The unit cell parameters were determined as a=15.55 Å, b=3.616 Å, c=10.13 Å, α=89.42 °, β=109.80 °, γ=89.50 °, and the lattice type was C-centered. The crystal system should be monoclinic. 2D slices 0kl, h0l and hk0, as cut from the reconstructed 3D reciprocal lattice, are shown as in Figure. S4B, II-IV. The systematic absences can be deduced as hkl: $h+k = 2n+1$; 0kl: $k = 2n+1$; h0l: $h = 2n+1$; hk0: $h+k = 2n+1$; h00: $h = 2n+1$ and 0k0: $k = 2n+1$. This gave the following three possible space groups: $C2/m$, Cm and $C2$. The RED results matched very well with the PXRD results. The crystallographic information is given in Table S1 and S2.
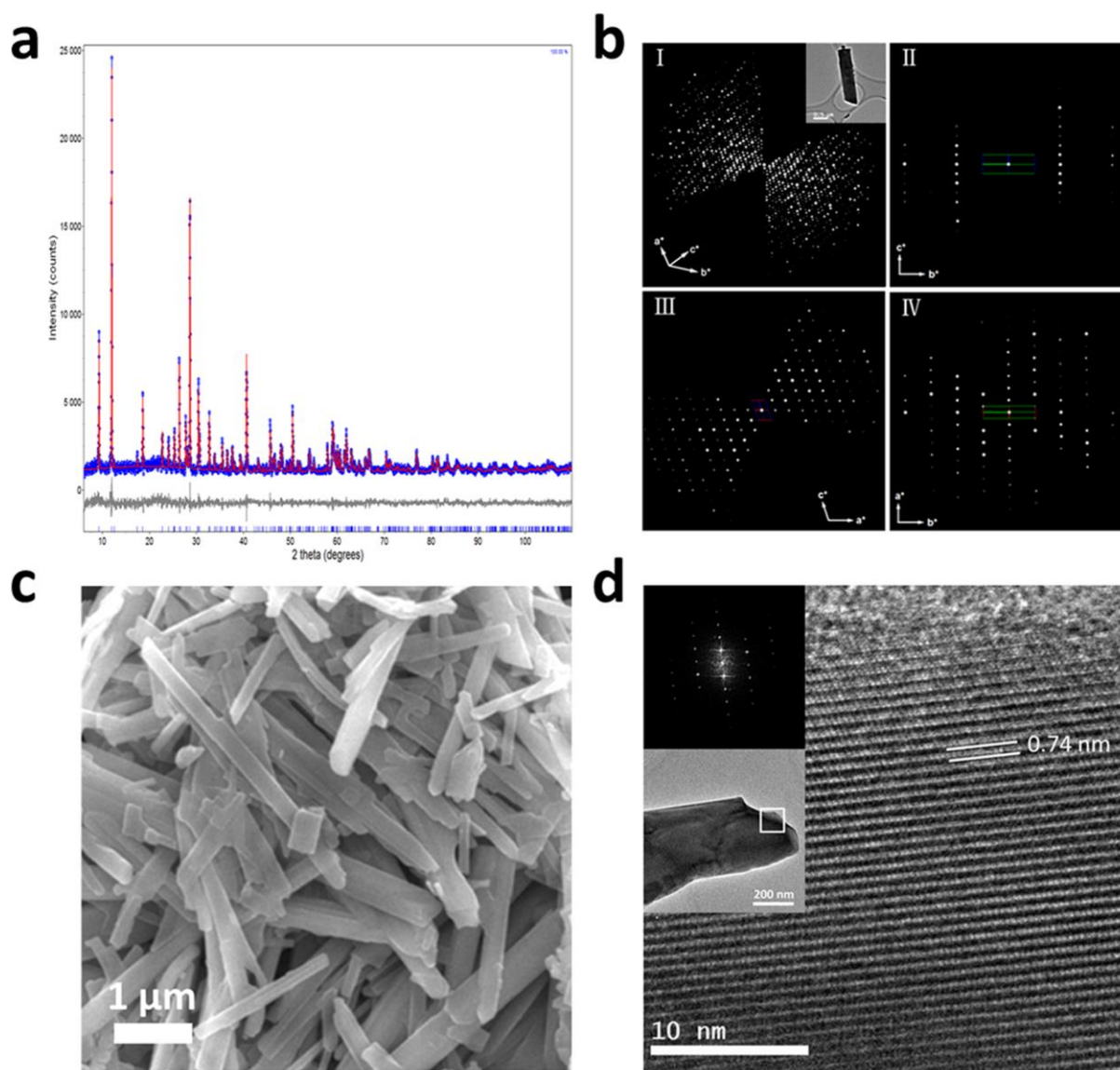
2. K-V-O

Figure S5. Crystal structure and morphology characterization of K-V-O nanowires. (a) Powder X-ray Rietveld refinement plot of K-V-O nanowires. The blue circles are for the observed data. The red solid line is for the calculated data. The grey solid curve is for the difference. The vertical bars indicate positions of the Bragg peaks. **(b)** The rotation electron diffraction (RED) data of a K-V-O nanowire. I represents 3D reciprocal lattice of the K-V-O nanowire reconstructed from the RED data and II-IV represent 2D the 0*kl*, *h*0*l* and *hk*0 slices cut from the reconstructed 3D reciprocal lattice. **(c)** SEM image of the K-V-O nanowires. **(d)** HRTEM image

from the area marked by a square in the inserted TEM image of a K-V-O nanowire showing that the layers are in parallel to the nanowire with the layer spacing of ~ 7.4 Å. The Fourier transform of the HRTEM image is also inserted.

Table S3. Crystallographic data, experimental conditions for powder X-ray diffraction data collection and results of the Rietveld analysis of K-V-O nanowires

Chemical formula of framework	$K_{0.70}V_6O_{15}$
Formula weight	573.01
Crystal system	Monoclinic
Space group	$C2/m$
a/Å	15.6702 (5)
b/Å	3.6150(1)
c/Å	10.1128(3)
β/°	109.214(2)
Cell volume/Å^3	540.95(3)
Z	2
Temperature/K	298(2)
Wavelength/Å	1.5418
2ϑ range/°	6.004 - 109.993
Number of points	6118
Number of reflections	415
Number of structural variables	82
Rp	0.0664
Rwp	0.0868
Rexp	0.0268
GOF	3.243

Table S4. Atomic coordinates, thermal parameters and occupancies of K-V-O.

Atom	x	y	z	Beq($Å^2$)	Occupancy
V1	0.33401(29)	0	0.10122(47)	2.54(18)	1
V2	0.11777(30)	0	0.11266(39)	3.57(19)	1
V3	0.28258(26)	0	0.40134(65)	3.65(20)	1
K	0.0064(13)	0	0.4145(21)	4.99(79)	0.350(14)
O1	0	0	0	3.82(19)	1
O2	0.1776(11)	0	-0.0564(20)	3.82(19)	1
O3	0.3645(13)	0	-0.0744(19)	3.82(19)	1
O4	0.43092(46)	0	0.23643(80)	3.82(19)	1
O5	0.2584(13)	0	0.2183(20)	3.82(19)	1
O6	0.08838(47)	0	0.25659(77)	3.82(19)	1
O7	0.2498(14)	0	0.5704(17)	3.82(19)	1
O8	0.39486(44)	0	0.4854(13)	3.82(19)	1

The PXPD pattern of K-V-O nanowires for Rietveld refinement was collected on a PANalytical X'Pert PRO MPD diffractometer in transmission geometry using Cu K_α radiation with the range 2θ = 6-110 °. The sample was packed into 0.5 mm diameter borosilica capillary. The Rietveld refinement was performed using Topas Academic V4.1. The initial V and O positions for the refinement were from the structure of $Na_{0.85}V_6O_{15}$, and the K position was found in the Fourier difference map during the refinement.

The rotation electron diffraction (RED) method was also applied on the K-V-O sample. 285 ED frames were collected with a step size of 0.40 °, covering a tilt range from -54.91 ° to 60.06 °. The

exposure time for each ED frame was 0.5 s. The three-dimensional reciprocal lattice was reconstructed from the ED frames using the RED software package and is shown in Figure S5B. The unit cell parameters were determined as a=15.62 Å, b=3.643 Å, c=10.15 Å, α=90.16°, β=108.55°, γ=89.49°, and the lattice type was C-centered. The crystal system should be monoclinic. 2D slices $0kl$, $h0l$ and $hk0$, as cut from the reconstructed 3D reciprocal lattice, are shown as in Figure. S5b,II-IV. The systematic absences can be deduced as hkl: $h+k = 2n+1$; $0kl$: $k = 2n+1$; $h0l$: $h = 2n+1$; $hk0$: $h+k = 2n+1$; $h00$: $h = 2n+1$ and $0k0$: $k = 2n+1$. These give the following three possible space groups: $C2/m$, Cm and $C2$. The RED results matched very well with the PXRD results.

3. Li-V-O

Figure S6. Crystal structure and morphology characterization of Li-V-O nanowires. (a) Profile fitting plot of Li-V-O nanowires. The blue circles are for the observed data. The red solid line is for the calculated data. The grey solid curve is for the difference. The vertical bars indicate positions of the Bragg peaks. (b) The rotation electron diffraction (RED) data of a Li-V-O nanowire. I represents 3D reciprocal lattice of the Li-V-O nanowire reconstructed from the RED data and II-IV represent 2D $0kl$, $h0l$ and $hk0$ slices cut from the reconstructed 3D reciprocal lattice. (c) SEM image of the Li-V-O nanowires. (d) HRTEM from the area marked by a square in the inserted TEM image of a Li-V-O nanowire showing that the layers are in parallel to the

nanowire with the layer spacing of ~ 7.2 Å. The Fourier transform of the HRTEM image is also inserted.

As the low atomic scattering factor of Li, it is difficult to find the position of Li cations by Rietveld refinement on Li-V-O sample. Therefore, only profile fitting was applied on Li-V-O sample. Full pattern decomposition was performed by Pawley refinement conducted in Topas V4.1 Acadaminc using data in the range $2\theta = 6\text{-}120°$. Background was fitted with a 10th order Chebyschev polynomial. The refinement was conducted using a PearsonVII peak profile function, followed by refinement of unit cells and zero-shift. The space group used for profile fitting is *C*2/*m*. The refined unit cell parameters are a=15.3883(8) Å, b=3.6045(2) Å, c=10.0808(5) Å and β=110.272(2)°, which match with the unit cell parameters of $Li_{0.9}V_6O_{15}$ in database (a=15.38(2) Å, b=3.60(2) Å, c=10.03(2) Å and β=110.70(25)°).

The rotation electron diffraction (RED) method was also applied on the Li-V-O sample. 420 ED frames were collected with a step size of 0.40°, covering a tilt range from -54.60° to 67.13°. The exposure time for each ED frame was 0.5 s. The three-dimensional reciprocal lattice was reconstructed from the ED frames using the RED software package and is shown in Figure S6B. The unit cell parameters were determined as *a*=15.49 Å, *b*=3.638 Å, *c*=10.054 Å, α=90.72°, β=109.53°, γ=89.49°, and the lattice type was *C*-centered. The crystal system should be monoclinic. 2D slices 0*kl*, *h*0*l* and *hk*0, as cut from the reconstructed 3D reciprocal lattice, are shown as in Figure S6B,II-IV. The systematic absences can be deduced as *hkl*: $h+k = 2n+1$; 0*kl*: $k = 2n+1$; *h*0*l*: $h = 2n+1$; *hk*0: $h+k = 2n+1$; *h*00: $h = 2n+1$ and 0*k*0: $k = 2n+1$. These give the following three possible space groups: *C*2/*m*, *Cm* and *C*2. The RED results matched very well with the PXRD results.
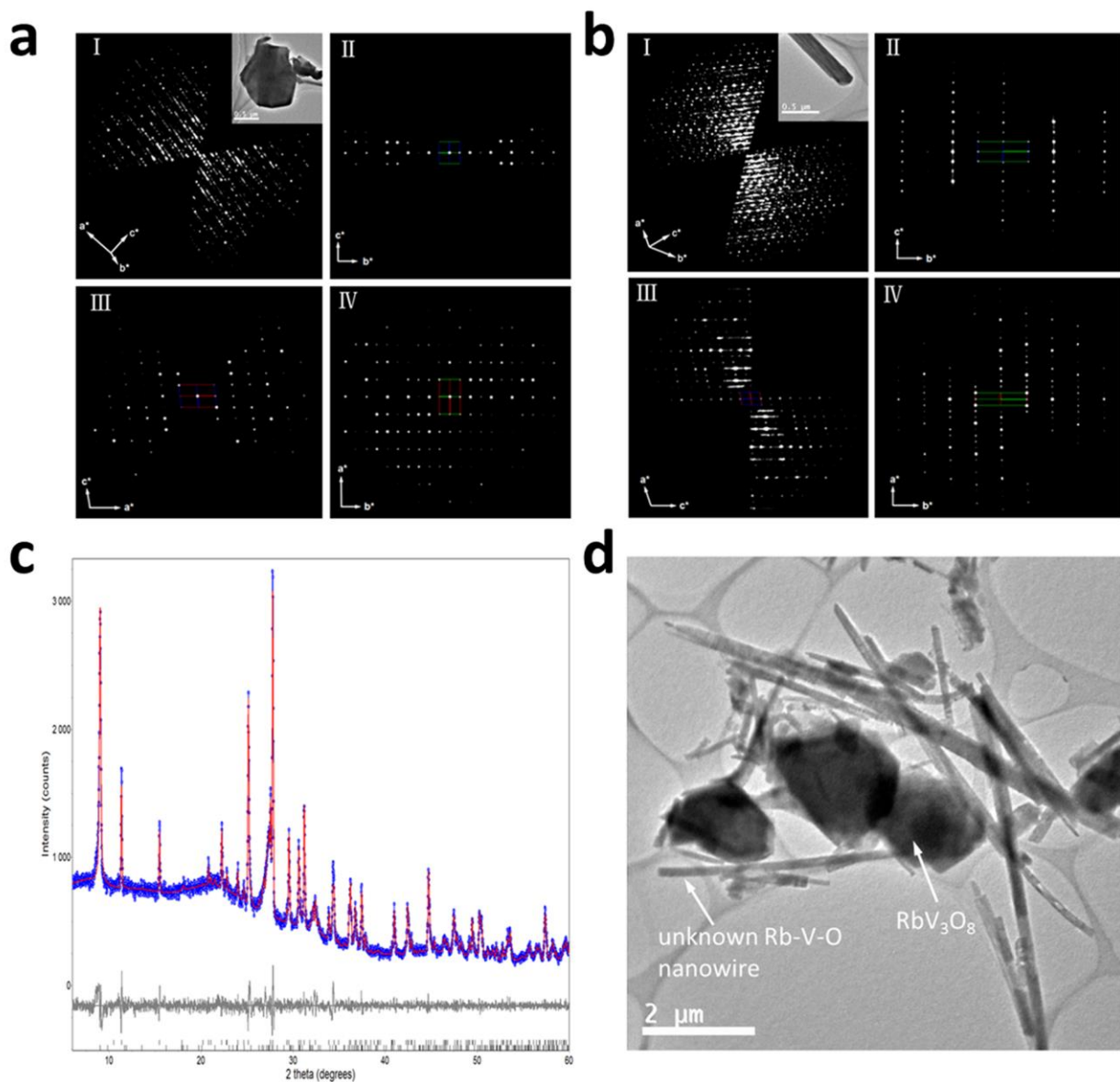
4. Rb-V-O

Figure S7. Crystal structure and morphology characterization of Rb-V-O sample. (a) The rotation electron diffraction (RED) data of a plate-like crystal RbV_3O_8. I represents 3D reciprocal lattice of the plate-like crystal reconstructed from the RED data and II-IV represent 2D $0kl$, $h0l$ and $hk0$ slices cut from the reconstructed 3D reciprocal lattice. (b) The RED data of a metastable Rb-V-O nanowire. I represents 3D reciprocal lattice of the nanowire reconstructed from RED data and II-IV represent 2D $0kl$, $h0l$ and $hk0$ slices cut from the reconstructed 3D reciprocal lattice. (c) Profile fitting plot of Rb-V-O sample. The blue circles are for the observed

data. The red solid line is for the calculated data. The grey solid curve is for the difference. The vertical bars indicate positions of the Bragg peaks (up: RbV_3O_8, and down: unknown Rb-V-O phase). (**d**) TEM image of Rb-V-O sample showing two types of crystal morphologies, plate-like and nanowires.

The TEM image of Rb-V-O sample showed two types of crystal morphologies in the sample, plate-like crystals and nanowires. If more than one phase is present in a sample, it is often challenging to determine the unit cell parameters by PXRD. The rotation electron diffraction (RED) method was used for the unit cell determination of both plate-like crystals and nanowires. For the plate-like crystal, 275 ED frames were collected with a step size of $0.40°$, covering a tilt range from $-49.70°$ to $61.37°$. The exposure time for each ED frame was 0.5 s. The three-dimensional reciprocal lattice was reconstructed from the ED frames using the RED software package and is shown in Figure S7A. The unit cell parameters were determined as $a=5.011$ Å, $b=8.391$ Å, $c=7.906$ Å, $\alpha=90.34°$, $\beta=96.08°$, $\gamma=89.86°$, and the lattice type was P-lattice. The crystal system should be monoclinic. 2D slices $0kl$, $h0l$ and $hk0$, as cut from the reconstructed 3D reciprocal lattice, are shown as in Figure S7A, II-IV. The systematic absences can be deduced as $0k0$: $k=2n+1$, and $00l$ reflections were in the missing cone. These give the following two possible space groups: $P2_1/m$ and $P2_1$. By checking the database, the unit cell parameters of the plate-like crystal match with those of RbV_3O_8 ($a=4.9864(8)$ Å, $b=8.442(1)$ Å, $c=7.8621(7)$ Å, $\beta=96.064(9)°$, and space group $P2_1/m$).

For the nanowires, 399 ED frames were collected with a step size of $0.40°$, covering a tilt range from $-60.46°$ to $55.00°$. The exposure time for each ED frame was 0.5 s. The three-dimensional reciprocal lattice was reconstructed from the ED frames using the RED software package and is shown

in Figure S7B. The unit cell parameters were determined as $a= 15.39$ Å, $b= 3.646$ Å, $c= 9.7048$ Å, $\alpha= 89.90°$, $\beta= 101.38°$, $\gamma= 89.42°$, and the lattice type was P-lattice. The crystal system should be monoclinic. 2D slices $0kl$, $h0l$ and $hk0$, as cut from the reconstructed 3D reciprocal lattice, were shown as in Figure S7B, II-IV. No systematic absences were observed. This gives the following three possible space groups: $P2/m$, Pm, and $P2$. No match of the space group and unit cell parameters was found in the ICDD database. Thus the nanowire phase may be a new phase. From the reconstructed 3D reciprocal lattice, some diffraction streaks can be found along the c^*-axis, which indicates possible stacking faults.

Profile fitting of the PXRD pattern of Rb-V-O sample was applied to confirm the two phases in the sample. Full pattern decomposition was performed by Pawley refinement conducted in Topas V4.1 Acadaminc using data in the range $2\theta = 6\text{-}60°$. Background was fitted with a 10th order Chebyschev polynomial. The refinement was conducted using a Pearson VII peak profile function, followed by refinement of unit cells and zero-shift. The refined unit cell parameters of RbV_3O_8 are $a= 4.9824(5)$ Å, $b= 8.4311(9)$ Å, $c= 7.8496(8)$ Å, and $\beta= 96.094(6)°$ with the space group $P2_1/m$, which match with the unit cell parameters of RbV_3O_8 in database very well. For the unknown nanowires, the unit cell parameters are $a= 15.142(3)$ Å, $b= 3.6069(9)$ Å, $c= 9.972(2)$ Å, and $\beta= 100.56(2)°$ with the space group $P2/m$. From the powder XRD pattern, some peaks show peak broadening, which is caused by the stacking faults in the nanowire phase.
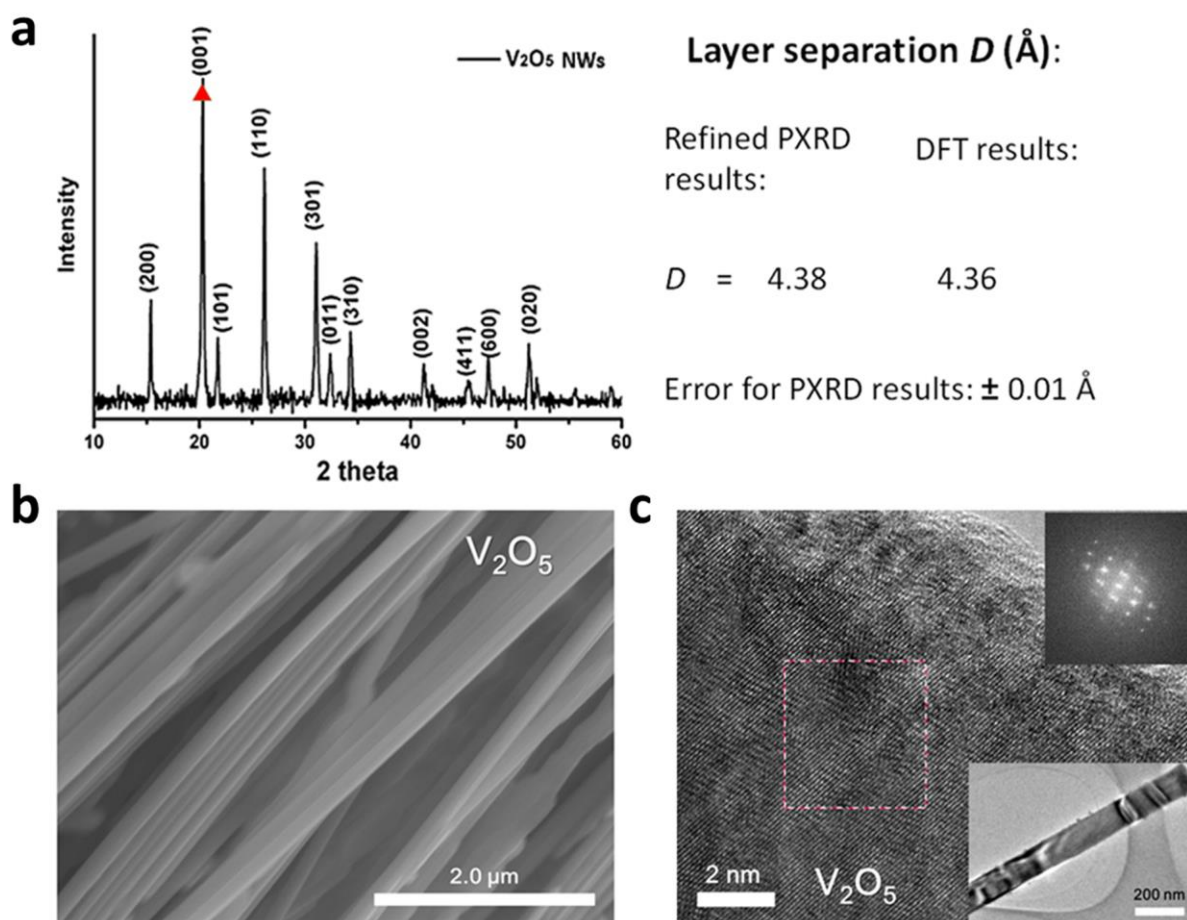
5. V_2O_5

Figure S8. Crystal structure and morphology characterization of V_2O_5 nanowires. (a) PXRD pattern of V_2O_5 nanowires. (Left) Obtained nanostructured materials correspond to pure phase V_2O_5. (Right) PXRD and DFT results of (001) interplanar layer separation, which agree well with each other. **(b,c)** SEM image and HRTEM image of V_2O_5 nanowires, respectively. The insets are the TEM image and the Fourier transform of the selected area in the HRTEM image.

6. *Details of diffusion barriers for A in A-V-O as well as Li in V_2O_5 and $K-V_2O_5$*

To qualitatively explain the experimentally observed remarkable cycling stability of large-ion pre-intercalated layered oxide materials as LIB cathode, we calculated diffusion barrier ($E_{barrier}$) of pre-intercalated A ions in A-V-O for a charge state without considering lithiated structure. We introduced an un-occupied site of A ion to a double-unit-cell model $A_8V_{48}O_{120}$ (for A = Li, Na and K, the unit cell of A-V_2O_5 is $A_4V_{24}O_{60}$), and then obtained the cell $A_7V_{48}O_{120}$ for the barrier calculations (see Fig. S9a,b). Similarly, in the case of A = Rb, the cell $Rb_{15}V_{48}O_{120}$ was used for the barrier calculations (the unit cell of Rb-V_3O_8 is $A_8V_{24}O_{64}$). The most likely diffusion paths only in the considered configuration were calculated. In this particular asymmetric model, there are two choices for the first step of the local diffusion of the pre-intercalated A ion (the middle yellow solid circle in Fig. S9b): to the nearest-next un-occupied site A or B. The results of the calculated barriers are shown in Table S5. For example, the barriers of K ion are 1.773 eV along the A direction, and 2.457 eV along the B direction, respectively. The barriers of pre-intercalated A ion diffusion can be related to cycling stability of A-V-O, which order well in agreement with the experimentally observed order of A-V-O cycling stability (Fig. 3). It should be noted that the adopted simplified theoretical treatments by considering the particular supercell structure, might not be adequate to quantitatively calculate diffusion barriers of A and Li ions, but should be enough to capture the leading physics of partial occupation.

Similarly, we have also performed calculations (Fig. S9c-f) on Li^+ diffusion barriers in V_2O_5 and $K-V_2O_5$ to further estimate the effects of pre-intercalated large ions, and the results are presented in Table S6. The Li ion diffusion barrier in $K-V_2O_5$ is lower than that in V_2O_5 when the Li ion does not pass the K ion, and is higher than the barrier in V_2O_5 when the Li ion passing the K ion. These results

suggest that the pre-intercalation of K ions to V-O layers can promote the Li-ion diffusion in the path without K ions, and hinder the Li-ion diffusion in the path with K ions. Although our treatment of Li ion diffusion is quite simplistic, it clearly shows that indeed large-ion pre-intercalation can not only improve the cycling stability of layered oxide materials like V_2O_5, but also promote the charge/discharge rate, which are consistent with our experimental findings.
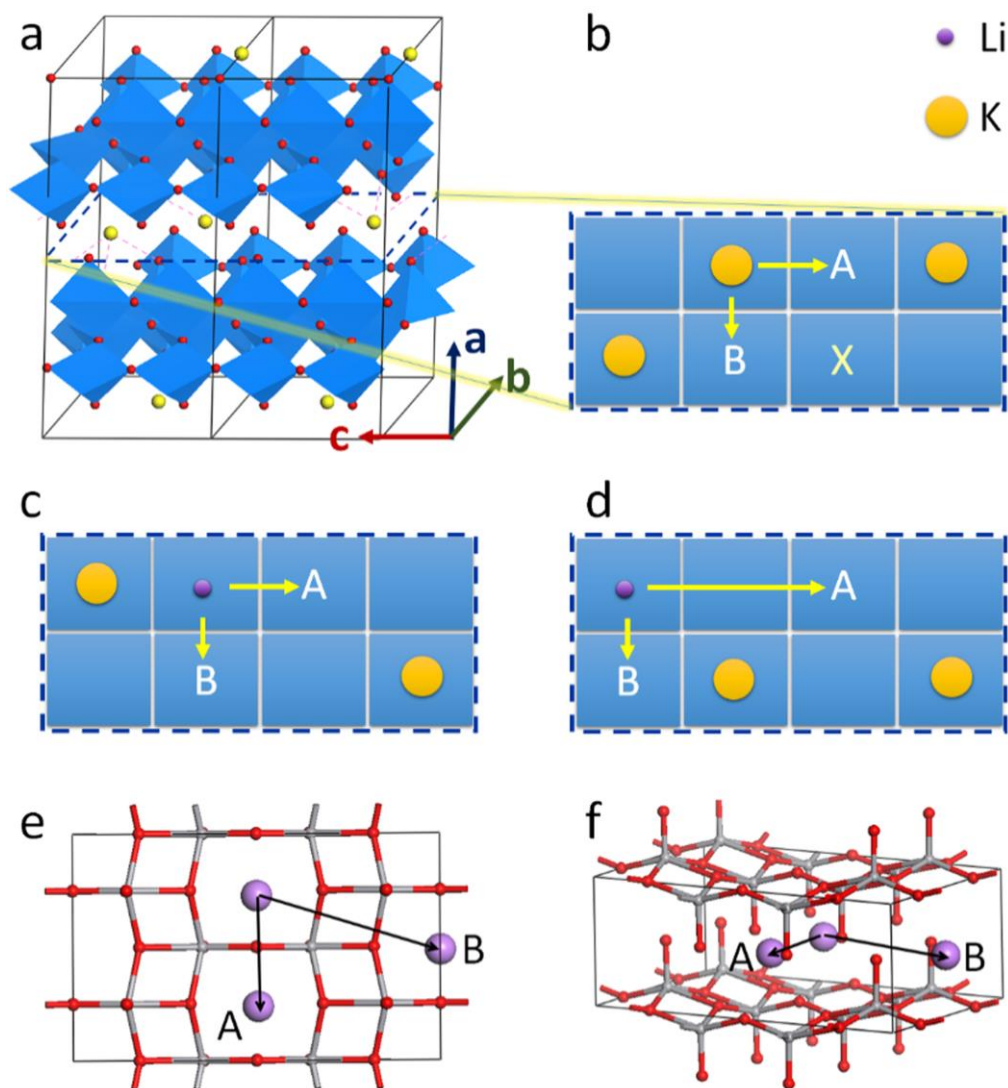

Figure S9. Schematic diagram of the cell applied for diffusion-barrier calculations. (a) The applied cell $A_7V_{48}O_{120}$ for barrier calculations when A = Li, Na and K. The yellow and red balls indicate the pre-intercalated A ion and the oxygen atom in V-O layers, respectively. **(b-d)**

Schematic diagram of the layer for the first step of the local diffusion of pre-intercalated A ion (**b**) and the diffusion of intercalated Li ion without (**c**) and with (**d**) passing the pre-intercalated A ion. The blue squares indicate the V-O layer structure, the yellow large and violet small solid circles denote the pre-intercalated A ion and the intercalated Li ion, respectively. The site X is initially un-occupied for A ion, by which we model the partial occupation of alkali ions A in A-V-O. (**e,f**) The top and side views of the cell applied for the diffusion-barrier calculation of Li ion in V_2O_5.

Table S5. Diffusion barriers of A ions along the directions A and B of A-V-O structure. The cell $A_7V_{48}O_{120}$ is applied for A = Li, Na and K, and the cell $Rb_{15}V_{48}O_{120}$ is used for A = Rb.

	Li (eV)	Na (eV)	K (eV)	Rb (eV)
Direction A	0.354	0.973	1.773	1.509
Direction B	0.512	1.302	2.457	2.643

Table S6. Diffusion barriers of Li ion along the directions A and B of V_2O_5 and $K-V_2O_5$ structures. The cell V_8O_{20} is applied for V_2O_5, and $K_6V_{48}O_{120}$ for $K-V_2O_5$.

	V_2O_5 (eV)	$K-V_2O_5$ (eV)	
		Non-Passing K	**Passing K**
Direction A	0.469	0.383	1.241
Direction B	1.429	0.402	--

7. Stability of Rb-V₃O₈ and Rb-V₂O₅

Table S7. Binding energy of Rb in Rb-V-O ($E_{binding}$(Rb)). The difference of the Rb binding energy between Rb-V_2O_5 and Rb-V_3O_8 reaches a large value of 3.216 eV, indicating that Rb-V_3O_8 is much more stable than Rb-V_2O_5.

	Rb-V_2O_5	Rb-V_3O_8
$E_{binding}$(Rb) (eV)	-1.943	-5.159

To compare the stability of Rb-V_3O_8 and Rb-V_2O_5, we calculated the binding energy of Rb in Rb-V-O by the formula,

$$E_{binding}(A) = E(A_4V_{24}O_{60}) - E(A) - E(A_3V_{24}O_{60}), \qquad (S1)$$

and

$$E_{binding}(A) = E(A_8V_{24}O_{64}) - E(A) - E(A_7V_{24}O_{64}), \qquad (S2)$$

where E refers to the total energy per formula unit, with A = Rb. $E(A)$ indicates the total energy of metallic alkali metal A as a reference state. The S1 equation is for Rb-V_2O_5, while the S2 equation for Rb-V_3O_8. As presented in table S7, the difference of the Rb binding energy between Rb-V_2O_5 and Rb-V_3O_8 reaches a large value of 3.216 eV, indicating that Rb-V_3O_8 is much more stable than Rb-V_2O_5.

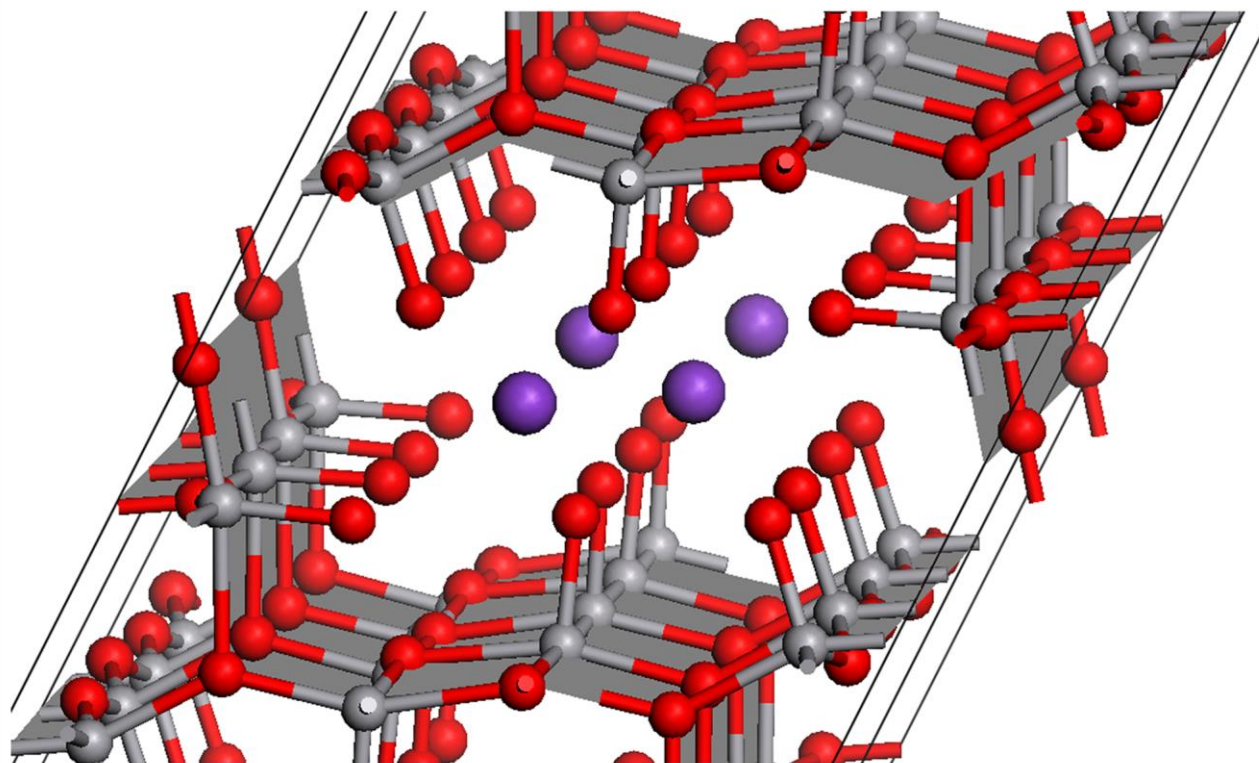## 8. Zoom in image of A-V-O

Figure S10. Zoom-in image of crystal structure for A-V-O (A=Li, Na, K).

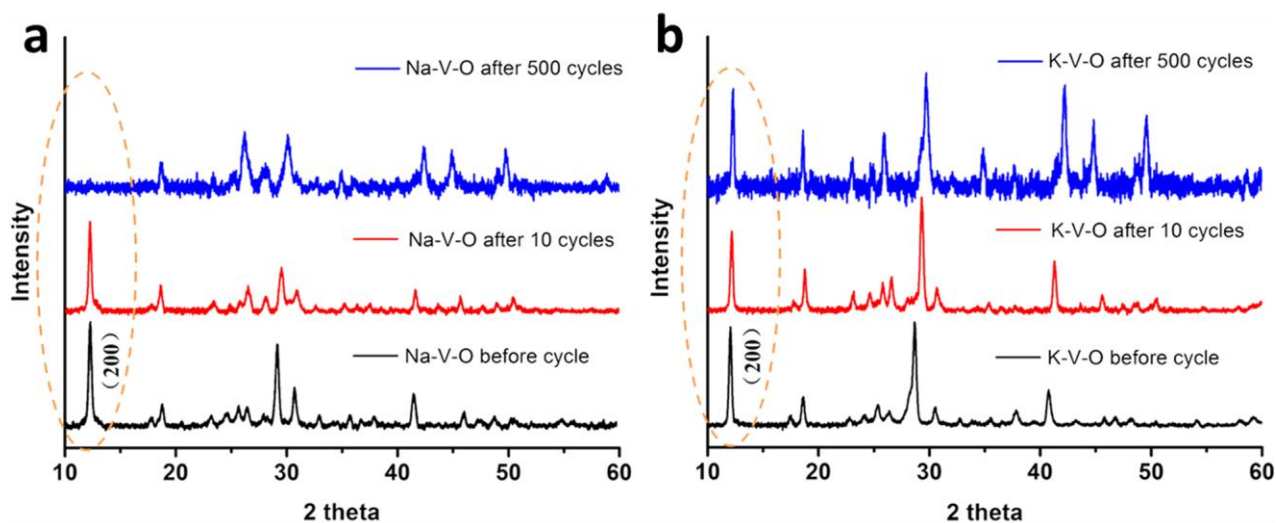## 9. *Comparison of the interlayer stability between Na-V-O and K-V-O*

Figure S11. XRD patterns of Na-V-O (a) and K-V-O (b) electrode before and after cycles at the same charge/discharge rate of 1 A/g in the potential range from 4.0 to 1.5 V vs. Li/Li$^+$.

As present in Fig. S11, it shows that after 500 cycles, the (200) reflection, characteristic of the layered structure, disappeared for Na-V-O but maintained well for K-V-O, revealing the collapse of interlayers in Na-V-O structure but not in K-V-O structure. Combined with the DFT results and atomic absorption spectroscopic analysis, it can be proved that K-ions can be selectively anchored between V-O layers, thus yielding more stabilized interlayers during charge-discharge process.

Part 4. Crystal structure, schematic representation, electrochemical properties and DFT analysis of A-M-O (A = Li, Na, K, Rb; M = Mo, Co, Mn, Fe-P)
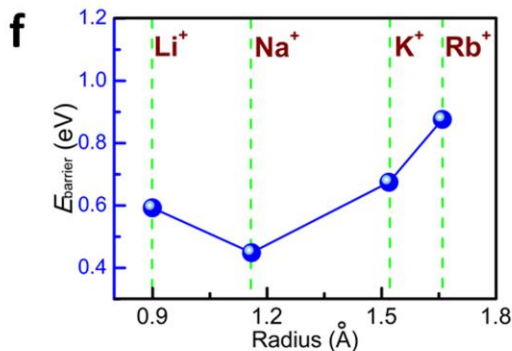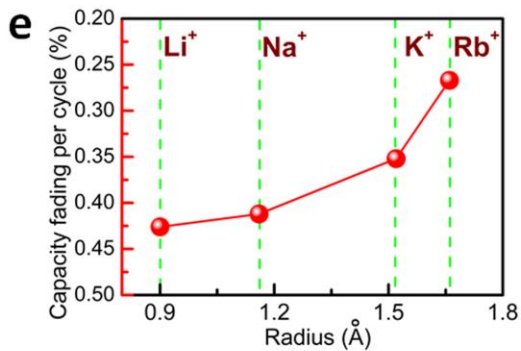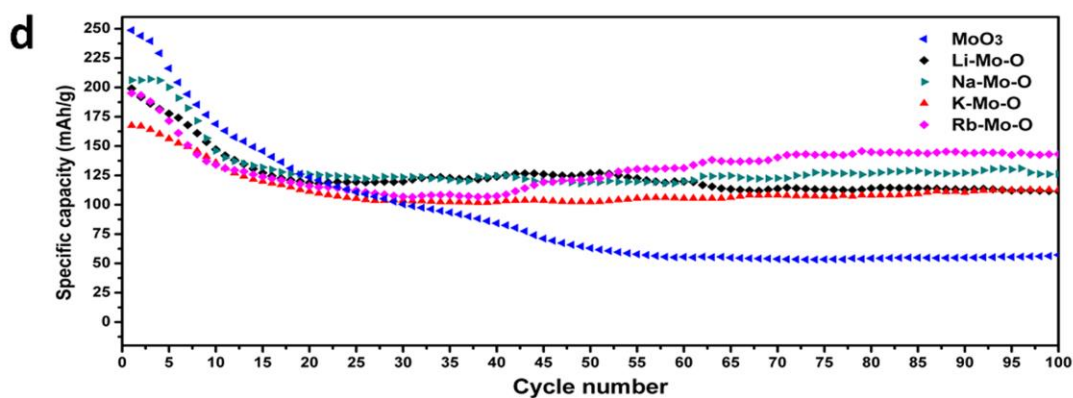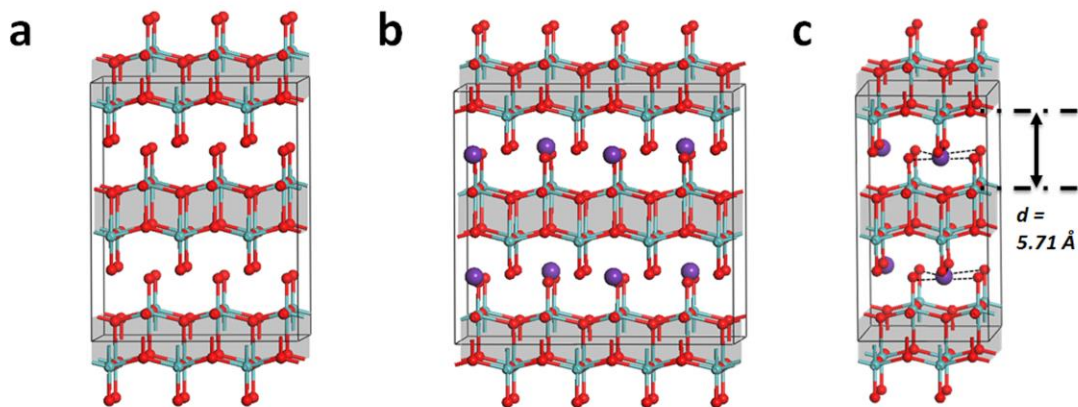
1. Details of A-Mo-O

Figure S12. Crystal structure, schematic representation, electrochemical properties and DFT analysis of A-Mo-O (A= Li, Na, K, Rb). (a,b) Illustrations of the crystal structure of MoO_3 and A-Mo-O. The red and purple balls represent oxygen and A atoms, respectively. (c) The size of ion diffusion channel of Rb-Mo-O. (d) The cycling performance of A-Mo-O at charge/discharge rate of 0.1 A/g in the potential range from 1.5 to 4.0 V *vs.* Li/Li$^+$. (e) Capacity fading per cycle vs. the radius of different pre-intercalated ions. (f) Diffusion barrier ($E_{barrier}$) of A in A-Mo-O obtained from DFT calculations.
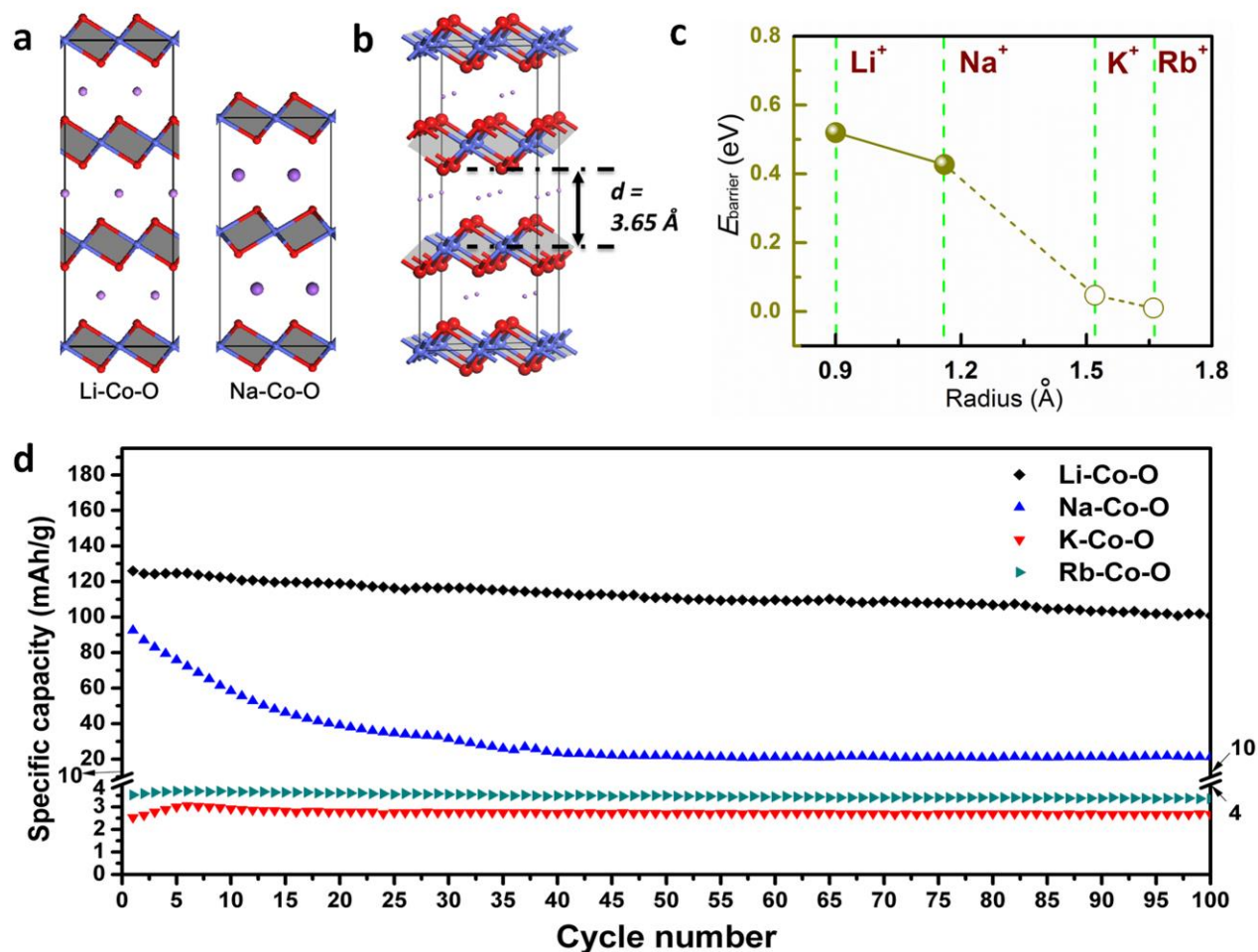
2. Details of A-Co-O

Figure S13. Crystal structures, DFT analysis and electrochemical properties of A-Co-O (A = Li, Na, K, Rb). (a) The crystal structure of Li-Co-O and Na-Co-O. The phases of obtained materials correspond to $LiCoO_2$ and $Na_{0.74}CoO_2$, respectively. (b) The size of ion diffusion channel of Li-Co-O. (c) Diffusion barrier ($E_{barrier}$) of A in A-Co-O obtained from DFT calculations. The circles indicate that the values are calculated based on the labile layered structures (the phases of K-Co-O and Rb-Co-O present no longer layered, which transformed to inactive materials). (d) The cycling performance of A-Co-O at charge/discharge rate of 0.1 A/g in the potential range from 2.0 to 4.2 V *vs.* Li/Li+.

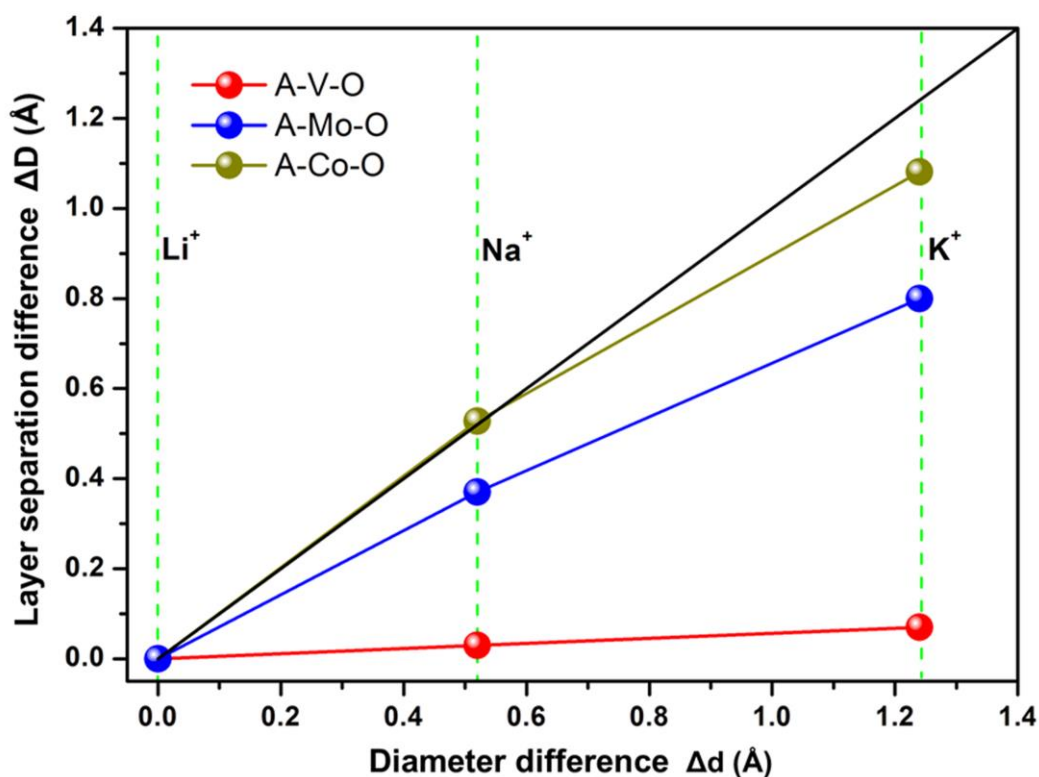### 3. Comparison between *ΔD* and *Δd*

Figure S14. Comparison between the layer separation difference ΔD (D_{A-M-O} - D_{Li-M-O}) of A-M-O and the diameter difference Δd (d_{A+} - d_{Li+}) of A ions. The origins of the horizontal and vertical axes represent the diameter of Li^+ and the layer separation of Li-M-O (M = V, Mo, Co), respectively. The vertical dashed lines denote the diameter difference between Li^+ and Li^+, Na^+ and Li^+, K^+ and Li^+, Rb^+ and Li^+, respectively. (All the layer separation values are obtained from DFT calculations.)

As represents in Fig. S14, the layer separation difference ΔD is much less than the corresponding diameter difference Δd for A-V-O and A-Mo-O, which is due to the presence of the flexible terminal oxygen atoms pointing to the interlayers. For A-Co-O, the ΔD is similar to the Δd, which is attributed to that the oxygen atoms are tri-connected on the surface of layer and are not flexible.
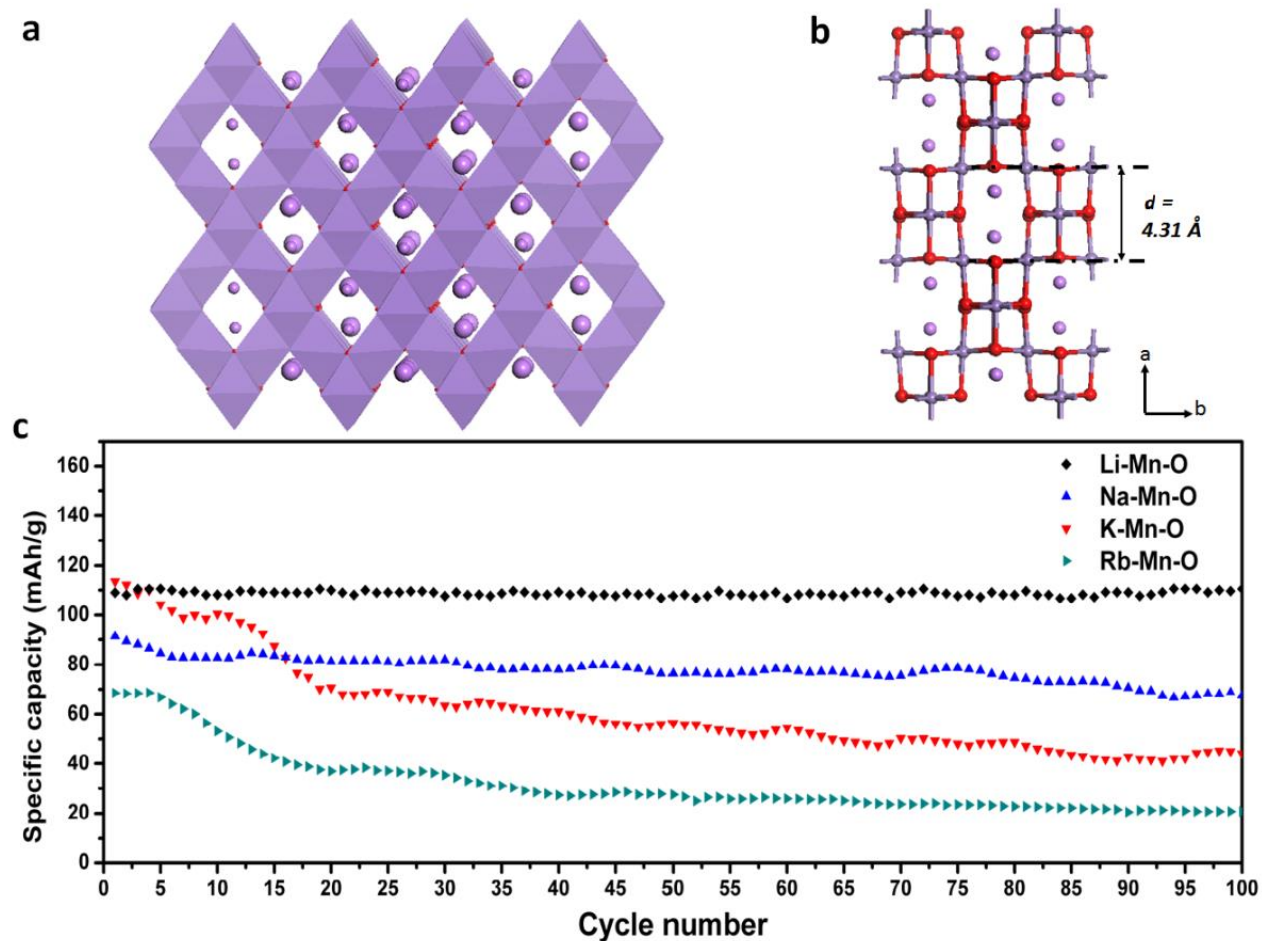
4. Details of A-Mn-O

Figure S15. Electrochemical properties of A-Mn-O (A= Li, Na, K, Rb). (a) Illustration of the crystal structure of Li·A-Mn-O. The large and small purple balls represent the A and Li atoms, respectively. (b) The size of ion diffusion channel of Li-Mn-O. (c) The cycling performance of A-Mn-O at charge/discharge rate of 0.1 A/g in the potential range from 2.0 to 4.5 V *vs.* Li/Li$^+$. Here, obtained nanostructured materials correspond to main phase A$_x$Mn$_2$O$_4$.
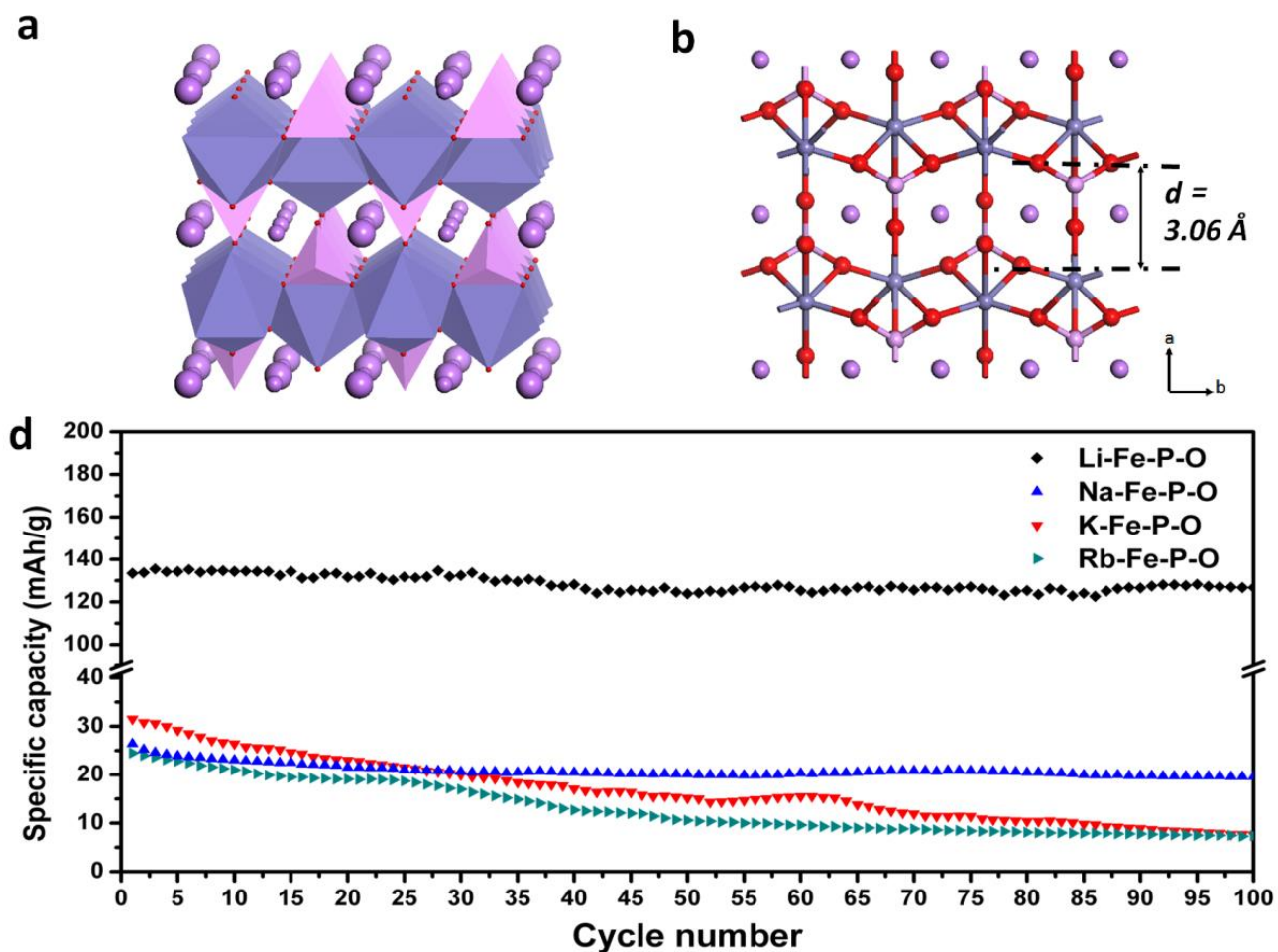
5. Details of A-Fe-P-O

Figure S16. Electrochemical properties of A-Fe-P-O (A= Li, Na, K, Rb). (a) Illustration of the crystal structure of Li·A-Fe-P-O. The large and small purple balls represent the A and Li atoms, respectively. (b) The size of ion diffusion channel of LiFePO$_4$. (c) The cycling performance of A-Fe-P-O at charge/discharge rate of 0.1 A/g in the potential range from 2.0 to 4.0 V *vs.* Li/Li$^+$. Here, obtained materials correspond to phases A$_x$FePO$_4$ and FePO$_4$.

Reference

(1) Kresse, G.; Hafner, J. *Phys. Rev. B* **1993,** *47*, 558.

(2) Kresse, G.; Furthmüller, J. *Phys. Rev. B* **1996,** *54*, 11169.

(3) Perdew, J. P.; Wang, Y. *Phys. Rev. B* **1992,** *45*, 13244.

(4) Perdew, J. P.; Ruzsinszky, A.; Csonka, G. I.; Vydrov, O. A.; Scuseria, G. E.; Constantin, L. A.; Zhou, X.; Burke, K. *Phys. Rev. Lett.* **2008,** *100*, 136406.

(5) Blöchl, P. E. *Phys. Rev. B* **1994,** *50*, 17953.

(6) Kresse, G.; Joubert, D. *Phys. Rev. B* **1999,** *59*, 1758.

(7) Hestenes, M. R.; Stiefel, E. *J. Res. Natl. Bur. Stand.* **1952**, 49, 409-436.

(8) Henkelman, G.; Uberuaga, B. P.; Jónsson, H. *J. Chem. Phys.* **2000,** *113*, 9901-9904.

(9) Sheppard, D.; Terrell, R.; Henkelman, G. *J. Chem. Phys.* **2008,** *128*, 134106.

(10) Sheppard, D.; Xiao, P.; Chemelewski, W.; Johnson, D. D.; Henkelman, G. *J. Chem. Phys.* **2012,** *136*, 074103.

(11) See http://theory.cm.utexas.edu/vtsttools/code/ for additional information and to obtain the VASP Transition State Theory code.

(12) Jónsson, H.; Mills, G.; Jacobsen, K. W. Classical and Quantum Dynamics in Condensed Phase Simulations (ed. Berne, B. J.; Ciccotti, G.; Coker, D. F.) 385-404 (World Scientific, Singapore, 1998).